Terrain Map Building for a Walking Robot Equipped with an Active 2D Range Sensor

Przemysław Łabęcki, Dawid Rosiński, Piotr Skrzypczyński

Abstract:

This paper deals with problems of rough terrain perception and mapping for walking robots equipped with inexpensive optical range sensors providing 2D data only. Two different sensing modalities are considered: the structured light sensor, and the Hokuyo URG-04LX laser scanner. Measurement uncertainty in both sensors is taken into account, and different geometric configurations of these sensors on the walking robot are analysed, yielding the configurations that are best for the task of terrain perception. Then, application of the acquired range data in local terrain mapping is presented. The mapping algorithm as well as novel methods for removing map artifacts that result from qualitative errors in range measurements are detailed. Experimental results are provided.

Keywords: *walking robot, laser scanner, structured light, sensor model, map building.*

1. Introduction

Nowadays, walking robots are increasingly employed in environments where the classic 2D maps are insufficient. A perceived terrain map is required by the robot's control system in order to avoid obstacles and to select safe footholds. However, in a walking robot the exteroceptive sensors have to be compact and light-weight. Although vision is a popular sensing modality in walking machines [9], active laser sensors offer more reliable terrain perception than most of the vision-based approaches, consuming usually a fraction of the computing power required by passive vision. Although laser scanning is now a matured robotics technology, the available 3D laser scanners are bulky, power consuming and expensive. On the other hand, the recently introduced technology of the time-of-flight (ToF) 3D cameras is still in its infancy, and does not offer enough reliability [20].
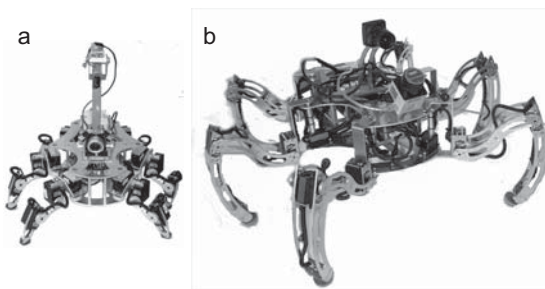

Fig. 1. Walking robots: Ragno (a) and Messor (b).

In order to overcome the above-mentioned limitations we experiment with active, laser-based 2D range sensors for terrain perception in walking robots. Distance measurements in laser range sensors are accomplished either by triangulation, or by the time-of-flight principle, which in turn can be implemented in several ways [1, 23]. A triangulation-based range sensor may be constructed adding a laser stripe projector to the on-board camera, which is present in the robot because of the requirements of the teleoperation interface [13], as it was shown on our small Ragno hexapod (Fig. 1a). This makes the range sensor lightweight and very cheap, but the structured light ranging principle has important drawbacks related to the ambient light [17]. Therefore, we experiment also with the Hokuyo URG-04LX 2D laser scanner as the terrain sensor on our bigger hexapod robot Messor (Fig. 1b). The URG series are new generation miniature laser scanners that unlike their older counterparts (e.g. the popular Sick LMS sensors) can be used on a middle-sized walking robot like Messor [3]. The scanner is tilted down, so the laser beam plane sweeps the ground ahead of the robot, enabling it to sense the terrain profile [15]. Both systems: the structured light sensor, and the tilted URG-04LX scanner provide only 2D data about a terrain stripe located in front of the robot. To obtain a terrain map the sparse range data have to be registered in a map using an estimate of the robot motion.

The aim of this paper is to discuss the issues related to terrain perception with 2D active sensors, and to show that sparse 2D range data can be efficiently used to build a local terrain map, which serves the purpose of safe feet placement. For this task a grid-type elevation map may be applied, which is easy to update in real-time, and can be directly used to select proper footholds [2]. However, an appropriate map updating algorithm is required, which takes into account the uncertainty of range measurements. In this paper the grid-based elevation map approach to the terrain mapping problem is employed for both sensing modalities under study. Basically, the same mapping algorithm is used, however, it turned out that depending on the sensing modality this algorithm has to be augmented with additional procedures that remove the map artifacts or spurious range data.

The remaining part of the paper is organized as follows. In Section 2 we discuss related work in terrain mapping from range data. Sections 3 and 4 describe in a unified manner the structured light sensor and the laser scanner, respectively. Section 5 describes our map building method. Section 6 reports experimental results and provides a comparison between mapping results achieved with the two sensing systems, and Section 7 concludes the paper.

2. Related work

Triangulation with laser light has been used in many different robotic systems before, addressing different ap-

plication areas, from assistive technology for vision impaired users [6], through affordable range sensing for commercial vehicles [17], to obstacle avoidance for planetary rovers [16]. However, this sensing modality was not used previously in a walking robot for terrain perception in any published work of which we are aware.

Laser scanners are widely used in mobile robotics, and were the subject of many analysis in the literature. However, the Hokuyo URG-04LX is a relatively recent development. As for now, a more detailed characterization of this laser scanner is given in [8] and [18]. Both papers analyze the dependency between the accuracy of distance measurements and the observed surface properties, distance to the target, and laser beam incidence angle. Moreover, [18] notices also the existence of mixed measurements produced by this sensor. The qualitative errors known as mixed measurements or "mixed pixels" are caused by the interaction of the laser beam with particular objects in the environment. They occur when the laser beam hits simultaneously two objects at different distances or two surfaces having different reflective properties [24].

The elevation map approach was used for the first time in [10], but it is used also on other robots working in rough terrain, e.g. the Lauron III [4], and the more recent Lauron IV [21] that builds a 2.5D height map holding both height and credibility values. This approach is similar to the one presented in this paper, but in [21] a ToF camera is used, that enables direct 3D perception, while we show that an elevation map can be built efficiently with sparse range data from the 2D range sensors. Sparse range data can be also used to estimate specific properties (shapes, dimensions) of a complex environment during walking or climbing, like in [11], but such an approach does not yield a terrain map that can be used for more general motion planning.

Recent research in terrain modelling resulted in methods that do not assume a fixed discretization of the space, such as the work of Plagemann *et al.* [19], which applies Gaussian process regression to the problem of uneven terrain mapping. While this approach is promising, enabling to fill-in large discontinuities that can appear in a map constructed with 3D data from a long-range sensor, it is computation-intensive, and cannot work in real-time on the embedded computer of our robot. In contrast, the map building system we present here is conceived as a source of information for the foothold selection module, and optimized for that purpose. A relatively small local map is built using a short-range 2D sensor specially configured to yield dense data from a limited area located in front of the robot. Thus, missing data can be filled-in by a much simpler method, while our goal is an artifact-free map that can be constructed on-board in real time.

3. Terrain perception with the structured light sensor

3.1. Structured light sensor

The motivation for using a structured light sensor on the small walking robot Ragno [25] stems primarily from the fact, that we wanted to use the on-board camera for teleoperation, but still be able to use it at the same time for ground profile acquisition supporting the foothold selection module [2]. The Ragno robot was equipped with the webcam-class colour camera Phillips NPC 1300/NC and a visible red light laser stripe emitter, forming together a structured light sensor. The laser stripe projector is an integrated unit obtained, together with the spherical lens and the electronics, from a dismantled commercial laser level tool.

The principle of operation of the triangulation-based range sensor is shown in Fig. 2. The laser beam is passed through a cylindrical lens, which defocuses it in the horizontal plane, but leaves it unaffected in the vertical direction. Thus, a light sheet is created, which intersects objects in front of the robot. If the laser sheet emitter is tilted down by the angle β, the light plane intersects the ground ahead of the robot, enabling it to sense the terrain profile.
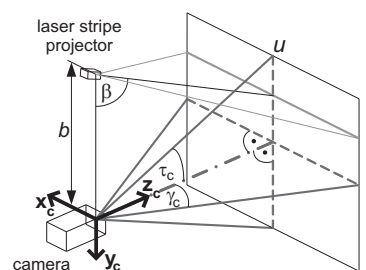

Fig. 2. Geometry of the structured light sensor and camera image.

A camera, which optical center is located at the distance b from the emitter perceives the stripe of laser light reflected by the illuminated surface. For the sake of simplicity we assume that the emitter is located within the plane of the camera CMOS sensor. The field of view of the camera is defined by the horizontal viewing angle $2\gamma_c$ and the vertical viewing angle $2\tau_c$. The relation between the location of points in the image u, v and the location of scene points x_c, y_c, z_c with regard to (w.r.t.) the camera coordinates is given by the equations:

$$z_c = \frac{b}{(1 - \frac{2v}{R_{\mathrm{ver}}})\tan\tau_c + \cot\beta}$$

$$x_c = z_c\left(1 - \frac{2u}{R_{\mathrm{hor}}}\right)\tan\gamma_c, \qquad (1)$$

$$y_c = -b\left(1 - \frac{\cot\beta}{(1 - \frac{2v}{R_{\mathrm{ver}}})\tan\tau_c + \cot\beta}\right),$$

where R_{ver} and R_{hor} are the vertical and horizontal size of the considered image (in pixels), respectively.

Equations (1) define a transformation from the image coordinate frame $[u\ v]^T$ to the 3D coordinates $[x_c\ y_c\ z_c]^T$. Parameters of this transformation are given by the vector $[b\ \beta\ \tau_c\ \gamma_c]^T$. These parameters should be known as precisely, as possible, so they are obtained by calibration. The main calibration procedure consists of two stages: the first one is a standard camera calibration procedure, while the second one is calibration of the geometric parameters of the emitter-camera system [14]. The latter calibration procedure provides the b and β parameters. When the actual focal length f and center of the image are known, a symmetrical region of interest window is defined, with the height R_{ver} and width R_{hor}. Using these parameters the

viewing angles τ_c and γ_c are computed:

$$\tau_c = \arctan\left(\frac{R_{\text{ver}}}{2f}\right), \quad \gamma_c = \arctan\left(\frac{R_{\text{hor}}}{2f}\right), \quad (2)$$

where f is given in pixels.

Detection of the laser stripe on the RGB camera image is accomplished by thresholding of the colour image, and then by elimination of the remained artifacts using some morphological operations performed on the binary image. This method was introduced in [12], and its slightly modified version used in our system is detailed in [13].

3.2. Measurement uncertainty of the structured light sensors

Main causes of errors in the measurements of the scene points location by means of the structured light sensor as well as sensitivity of the measurements to the parameters of the camera-projector system are analysed in [13]. Details of the error propagation procedure are given in [14].
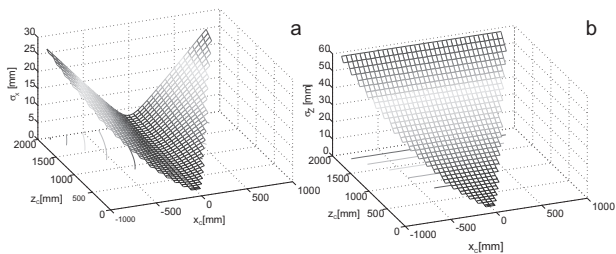

Fig. 3. Uncertainty depending on the location of a point w.r.t. the sensor coordinates.

Here we focus on the spatial resolution of the structured light sensor, which is important for the proper choice of the geometric configuration of the sensor mounted on the robot. This resolution depends on the resolution of the camera, and on the distance between the camera and the measured point [13, 14]. Figure 3 shows the analytically obtained dependence between the location of the measured point and the spatial uncertainty of the measurement for an example sensor configuration: VGA image resolution, $b = 100$ mm, $\beta = 70°$, $\tau_c = 19.1°$, $\gamma_c = 24.8°$. Because the y_c and z_c coordinates are coupled – they both depend only from v (1) – the uncertainty is shown only w.r.t. the $x_c z_c$ plane, while the camera is assumed to be at the $x_c = 0, z_c = 0$ coordinates. The uncertainty along the x_c axis grows only slightly with the distance from the sensor, but depends on the lateral distance from the camera optical axis (Fig. 3a). In contrary, the uncertainty along the z_c axis grows hyperbolically with the growing distance from the sensor (Fig. 3b).

3.3. Sensor configuration

Unfortunately, in a triangulation-based range sensor the parameters required for high resolution and low uncertainty of the measurements conflict with the requirements as to the field of view and operational characteristics. Thus, the final sensor design must be a compromise.

In order to reduce the uncertainty the spatial resolution of the measurements should be improved by decreasing the distance along the z_c axis between the measured point and the camera. To implement this we can decrease the β angle, or tilt the whole sensor by some α angle (Fig. 4a and b).
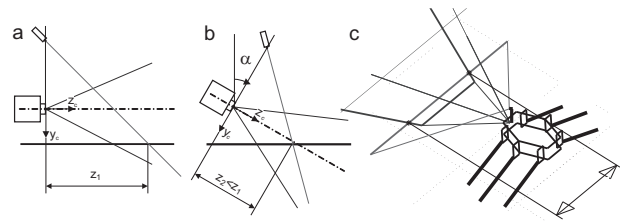

Fig. 4. Tilting the sensor towards the ground.

Because the robot uses the obtained terrain map mainly for foothold selection, it makes sense to configure the sensor in such a way that a relatively small area immediately ahead of the robot is measured with good resolution. However, a constraint is the field of view along the x_c axis. The robot should perceive a stripe of terrain wide enough to put all feet on the known ground (Fig. 4c).

An advantage of a sensor that is tilted towards the ground is reduction of mutual occlusions between the observed obstacles on an uneven terrain. Figure 5 presents results of a simulation of a robot equipped with the structured light sensor moving through a random stepfield consisting of boxes of various height. Multiple occlusions between the boxes cause many missing distance measurements (Fig. 5a). Decreasing the β parameter by $10°$ reduces the number of occlusions, and reduces the uncertainty of range measurements, which is coded by the grayscale level of the simulated laser stripe (Fig. 5b). Tilting the sensor by α=10° (instead of decreasing the β parameter) reduces the occlusions and uncertainty of the measurements even a little more (Fig. 5c). However, both of those configurations make the observed area of the ground more narrow.

Considering all these constraints, we chose the final set of parameters for the structured light sensor prototype mounted on the Ragno robot: $\tau_c = 28.14°$, $\gamma_c = 38.8°$, $b = 120$ mm, $\beta = 45°$, and $\alpha = 10°$. When the Ragno robot assumes its neutral posture the camera is located 17.4 cm above the ground, which results in the maximum measured range of 29.4 cm (on the ground plane).

4. Terrain perception with the laser scanner
4.1. URG-04LX scanner

In most of the laser scanners the distance is measured either by directly determining the time of flight of an emitted laser pulse traveling to a target and then reflected back (ToF principle), or indirectly, by determining the phase-shift between an amplitude modulated continuous wave and its reflection.

The Hokuyo URG-04LX 2D laser scanner exploits the phase-shift-based ranging technique. The range to the target object r is proportional to the measured phase shift ϕ_d:

$$r = \frac{c}{4\pi f_{AM}}\phi_d = \frac{1}{2}\lambda_{AM}\frac{\phi_d}{2\pi}, \quad (3)$$

where f_{AM} is the modulation frequency, λ_{AM} is the wavelength of the modulation, and c is the speed of light. Since ϕ_d is determined modulo 2π, the range measurement is unambiguous only within the distance $r_u = \frac{1}{2}\lambda_{AM}$ from the sensor. The URG sensor uses two different modulation frequencies in order to overcome this ambiguity. Thus, it achieves both good distance measurement resolution of
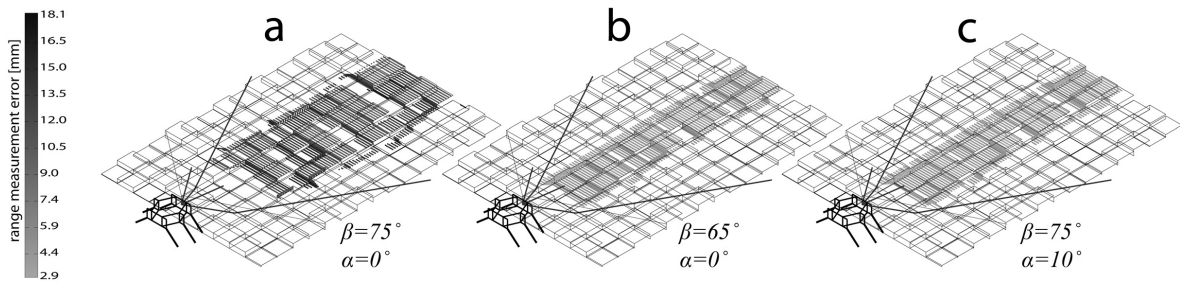
Fig. 5. Simulation of three configurations of the structured light system.

1 mm and a satisfactory maximum range of 4.095 m [7]. The scanner produces 683 measurements per revolution within the angular range of 240°. Complete scans are taken with a frequency of 10 Hz. The sensor weighs only 160 g and has a size of $50 \times 50 \times 70$ mm.

The URG-04LX specification defines its distance measurement accuracy for a white sheet of paper as 10 mm between 20 mm and 1000 mm, and 1% of the measured distance between 1 m and 4 m. As a range sensor based on the phase-shift principle the URG-04LX is characterized by a coupling between the accuracy of the measured distance and the received signal intensity. This coupling introduces important systematic errors into the distance measurements, which cannot be calibrated as in [1], because the URG scanner (at least with the standard software) does not allow for direct signal intensity measurements.

Both [8] and [18] propose calibration models for reducing the systematic errors. However, the linear model of [18] results in large residual distance errors whenever it is used in terrain mapping to correct distances smaller than 1000 mm at incidence angles of about 30°. Also the model given in [8] is not applicable, as it tries to describe the behaviour of the range measurements up to 4000 mm with one non-linear function, which makes its precision insufficient.
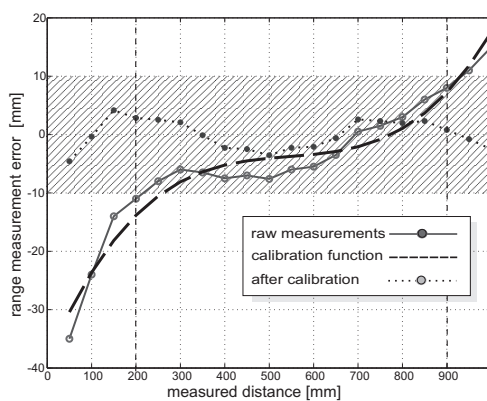

Fig. 6. Calibration of the URG-04LX measurements.

Therefore we have established our own calibration model, which is intended to capture behaviour of the URG sensor in the application of terrain profile acquisition. The experiment was performed with a grey paper target (R=G=B=128) for the incidence angle of 30°, and the measured distances from 50 to 1000 mm. The results of range measurements are shown in Fig. 6 using a solid line, with the third order polynomial calibration curve overlaid

using a dashed line. The resulting calibration is given as:

$$
\begin{aligned}
r &= r_m + \Delta r_m, \\
\Delta r_m &= 38.6 + 0.18 r_m + \\
&\quad + 0.3 \times 10^{-3} r_m^2 - 0.2 \times 10^{-7} r_m^3,
\end{aligned}
\tag{4}
$$

where r_m and r are the raw and the corrected range measurement, respectively. The calibration procedure given by (4) is valid only for the interval of distances from 50 mm to 1000 mm, but it is precise enough for the specific application of terrain perception. For instance, the systematic error of the corrected measurements is kept within the boundaries specified by the sensor's manufacturer, as shown in Fig. 6 by the dotted line that fits within the slanted area.

4.2. Sensor configuration

The mechanical design of the robot platform gives a possibility for two different variants of the sensing system [3]. The first one has the URG scanner attached between the two aluminium plates constituting the chassis (Fig. 8a), while in the second variant the scanner is mounted on the upper deck plate (Fig. 8b).

There are few sensor-specific requirements which should be taken into account when configuring the system. It was found in [18] that some targets produce specular reflections, but for most matted-surface targets these errors are insignificant if the incidence angle is smaller than 30°. Considering this result we configured our URG sensor in such way that the parts of terrain most interesting for the placement of robot feet, i.e. nearly-flat, horizontal surfaces are perceived with small incidence angle. Another concern is the non-linearity of the measurement errors in function of the distance. The sensing system configuration should ensure that target surfaces of heights from -10 to 15 cm (with regard to the local ground level), which can be climbed by the Messor robot will appear at distances falling into the most favorable range interval from 200 to 900 mm, which ensures lowest measurement errors (cf. Fig. 6).

Considering the above-mentioned requirements, we simulated three different configurations of the terrain profile sensing system. The first one (Fig. 7a) with the scanner mounted at the height of $d_z = 16$ cm and the pitch angle $\alpha = 15°$, the second one (Fig. 7b) with the scanner mounted at the height of $d_z = 26$ cm and the angle $\alpha = 20°$, and the third one (Fig. 7c), which has the scanner mounted also on the upper deck of the robot, but at the angle of 35°. The simulations present a walking robot equipped with the URG-04LX sensor in the three mentioned configurations moving through a randomly generated terrain.
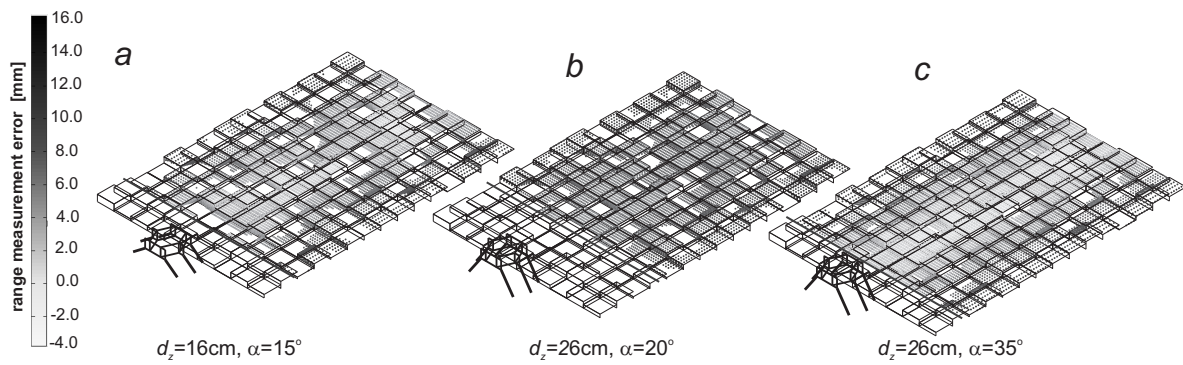
Fig. 7. Simulation of three configurations of the Hokuyo-based sensing system.
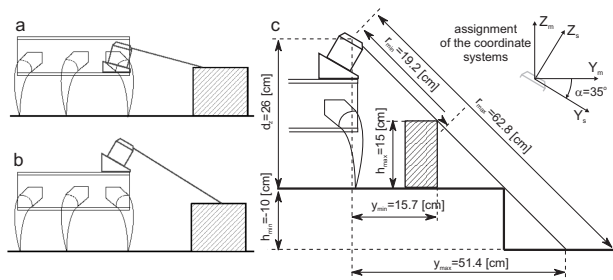

Fig. 8. Two variants of the terrain sensing system design (a,b), and geometry of the sensing system on the Messor robot (c).

The systematic error of range measurements is coded by the grayscale level of the simulated laser footprints on the observed objects. This error is computed according to the model given by (4). As it can be seen from Fig. 7a the first configuration of the sensor causes multiple occlusions between the obstacles, and as a result many missing distance measurements. Putting the sensor on the upper deck of the robot increases the field of view and reduces the number of occlusions, but increases the range measurement errors, as the observed obstacles are located too far (Fig. 7b). Tilting the sensor by $\alpha=35°$ further reduces the number of occlusions, and alse reduces the uncertainty of range measurements (Fig. 7c), as in this configuration the ground is closer to the sensor along the line of sight.

Although the increased pitch angle makes the observed area of the ground more narrow and reduces the look-ahead distance, these drawbacks are less profound in our application: the observed ground stripe is still wide enough to put the robot's feet on it, while the look-ahead distance is not so important because the robot uses the terrain map for foothold selection rather than for dynamic obstacle avoidance. Thus, it makes sense to configure the scanner in such a way that a small area immediately in front of the robot is perceived with high accuracy and without much occlusions. Therefore we finally attached the URG-04LX scanner to the upper deck of our robot at the height of $d_z = 26$ cm, and the pitch angle of $\alpha = 35°$ (Fig. 8c).

5. Map building method

5.1. Local terrain map concept

In the elevation grid map each cell holds a value that represents the height of the object at that cell [10]. However, a classic elevation map provides no means to com-

pensate such undesirable effects as missing data and range measurement artifacts. Therefore, we developed a map updating method, which is inspired by the algorithm of Ye and Borenstein [26], originally conceived for a wheeledd vehicle with the Sick LMS 200 scanner. The terrain map consists of two grids of the same size: an elevation grid and a certainty grid. The elevation grid holds values that estimate the height of the terrain, while each cell in the certainty map holds a value that describes the accuracy of the corresponding cell's estimate of the elevation. A sensor-centered local grid of the size 100×100 cells is used. The cell size varies depending on the sensor and the walking robot used. For the Ragno robot with the structured light sensor the cell size is 5×5 mm, while for the bigger Messor robot cells of the size 10×10 mm or 15×15 mm are used, depending on the expected self-localization uncertainty.

The local map that integrates the sparse range measurements moves with the robot always covering its surroundings. As in [26] it is assumed that an estimate of the 6-d.o.f. robot pose is available. For a legged robot such an estimate is not easy to obtain. The sparse data from the 2D range sensors we use cannot be employed for that purpose, because there is a lack of any significant overlapping between the new measurements and the recently perceived part of the terrain. For small local maps centered in the robot coordinates, and used for foothold selection the proprioceptive sensing exploiting the feet contacts and the Inertial Measurement Unit (IMU) is enough [5], while for exploration of more extended areas a vision-based SLAM (Simultaneous Localization and Mapping) procedure can be used [22].

5.2. Map updating algorithm

Regardless of the sensing modality used (i.e., structured light or 2D scanner) the range measurements are converted to 3D-points $\mathbf{p}_s$ in the sensor coordinate frame, then transformed to the map coordinates by using the robot pose estimate, and finally projected onto the 2D grid map:

$$\mathbf{p}_m = \mathbf{T}_s^m \mathbf{p}_s, \qquad (5)$$
$$\mathbf{T}_s^m = \mathrm{Rot}(X_m, \varphi_r)\mathrm{Rot}(Y'_m, \psi_r)\mathrm{Rot}(X''_m, \alpha),$$

where $\mathbf{p}_s=[x_s\ y_s\ z_s]^T$ and $\mathbf{p}_m=[x_m\ y_m\ z_m]^T$ are coordinates of the measured point in the sensor and the map frame, respectively. The homogeneous matrix $\mathbf{T}_s^m$ describes the transformation from the sensor frame to the map frame. This transformation consists of three rotations: the pitch φ_r and roll ψ_r angles of the robot trunk, and the α angle

that represents the constant pitch angle of the sensor w.r.t. the robot frame. These rotations are shown in Fig. 9a,b, and c respectively, for a robot with the laser scanner, but they are the same for the structured light sensor.
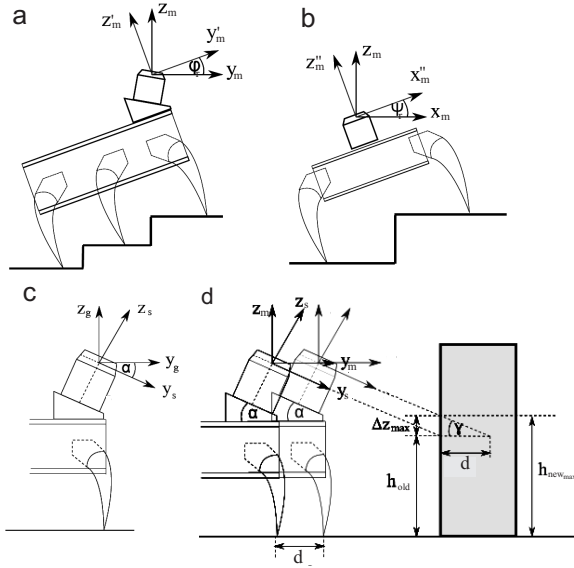

Fig. 9. Kinematic transformations of the measurements (a, b, c) and maximum change of elevation (d).

Once the measured points are available in the map coordinates, a plausibility assessment is accomplished in order to check if a newly obtained measurement is consistent with the existing elevation map and the constraints imposed by the movement of the robot. To this end a prediction of the maximum instantaneous change of elevation is used (Fig. 9d). For every two consecutive measurements r_k and r_{k+1}, the change of elevation $\Delta z_{\max}$ in a given cell of the map is computed taking into account the range measurement uncertainty, and the uncertainty of robot pose estimate.

For the laser scanner sensor this prediction is given by:

$$\Delta z_{\max} = d_{(k,k+1)} \tan \gamma + \left| \frac{\partial z_m}{\partial r} \Delta r \right| + \left| \frac{\partial z_m}{\partial \psi_r} \Delta \psi_r \right| +$$
$$+ \left| \frac{\partial z_m}{\partial \varphi_r} \Delta \varphi_r \right| + \left| \frac{\partial z_m}{\partial \alpha} \Delta \alpha \right|, \quad (6)$$

where z_m is the measured elevation of the observed point computed from (5), $d_{(k,k+1)}$ is a horizontal translation of the robot from k to $k+1$ time stamp, and γ angle is the total rotation of the trunk w.r.t. the X_m axis, which is obtained from the elements of the $\mathbf{T}_s^m$ matrix:

$$\gamma = \mathrm{atan2} \left(\frac{\cos \varphi_r \sin \alpha + \sin \varphi \cos \alpha \cos \psi_r}{-\sin \varphi_r \sin \alpha + \cos \varphi \cos \alpha \cos \psi_r} \right). \quad (7)$$

The values of $\Delta \varphi_r$, $\Delta \psi_r$ and $\Delta \alpha$ are maximum errors of the respective angles, while Δr is the laser scanner range measurement error, which is computed upon the sensor model (4). The value of $\Delta \alpha$ is $1°$ (a constant), but the values of $\Delta \psi_r$ and $\Delta \varphi_r$ depend on the accuracy of the IMU sensor used in the robot.

For the structured light sensor this prediction is slightly more complicated:

$$\Delta z_{\max} = d_{(k,k+1)} \tan \gamma + \left| \frac{\partial z_m}{\partial b} \Delta b \right| +$$
$$+ \left| \frac{\partial z_m}{\partial \beta} \Delta \beta \right| + \left| \frac{\partial z_m}{\partial \tau_c} \Delta \tau_c \right| +$$
$$+ \left| \frac{\partial z_m}{\partial b} \Delta b \right| + \left| \frac{\partial z_m}{\partial v} \Delta v \right| +$$
$$+ \left| \frac{\partial z_m}{\partial \psi_r} \Delta \psi_r \right| + \left| \frac{\partial z_m}{\partial \varphi_r} \Delta \varphi_r \right| +$$
$$+ \left| \frac{\partial z_m}{\partial \alpha} \Delta \alpha \right|, \quad (8)$$

because the term giving the dependence between the uncertainty of the measured elevation and the range measurement uncertainty is replaced by four elements describing how the uncertainty of the perceived elevation depends on the errors in parameters of the camera-projector system (1). The values of Δb, $\Delta \beta$, and $\Delta \tau_c$ are determined during the calibration procedure [14]. The Δv value is an estimate of the error in the vertical location of the laser stripe image on the camera matrix.

The maximum elevation change given by (6) is valid only if the robot is moving along a straight line. However, the walking robot often changes its orientation (the yaw angle θ_r) during motion because it has to put its feet at proper footholds. To enable computation of the $\Delta z_{\max}$ while changing the orientation, the idea given in [26] is extended to include also the turning motion. We assume that the robot observes an obstacle of constant elevation, and turns by an angle of θ. Hence, the distance between the two points being observed by the sensor, p and p' can be computed from the intersection of the straight lines at p', provided that the location of p is known (Fig. 10). Because we are interested only in the distance increment, without loss of generality we can let $x_p = 0$, and compute the distance as $\Delta x = x_{p'} = (r + d_s) \tan(\theta/2)\mathrm{sgn}(\theta)$. Then, the instantaneous horizontal translation of the sensor is computed: $d_{(k,k+1)} = \Delta x \tan(\theta)$, and used in (6) or (8).
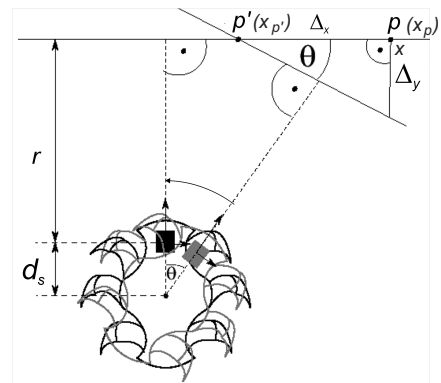

Fig. 10. Determination of the elevation change while turning.

A cell in the elevation map is denoted as $h^{[i,j]}$, and a cell in the certainty map as $c^{[i,j]}$. Whenever a new measurement

is available cells in the certainty map are updated at first:

$$c_{(k+1)}^{[i,j]} = \begin{cases} c_{(k)}^{[i,j]} + a & \text{if } |h_{m(k+1)} - h_{(k)}^{[i,j]}| \leq |\Delta z_{\max(k)}| \\ & \text{or } c_{(k)}^{[i,j]} = 0 \\ c_{(k)}^{[i,j]} & \text{otherwise,} \end{cases}$$

(9)

where a is the increment of the certainty value, and h_m is the elevation of the measured point, computed as $h_m = z_m + d_z + h_{\text{ref}}$ taking into account the current height of the robot d_z (it is computed upon the angles measured in joints), and the reference elevation h_{ref} at which the robot is located (obtained from the already created part of the map). Next, cells in the elevation map are updated:

$$h_{(k+1)}^{[i,j]} = \begin{cases} h_{m(k+1)} & \text{if } h_{m(k+1)} > h_{(k)}^{[i,j]} \\ h_{(k)}^{[i,j]} & \text{otherwise.} \end{cases}$$

(10)

5.3. Removal of artifacts and mixed measurements

The main advantage of the elevation map variant proposed by Ye and Borenstein [26] is the built-in mechanism for filtering of the artifacts. This mechanism is known as the Certainty Assisted Spatial (CAS) filter, and it employs the constraints on the spatial continuity of both the elevation map and the certainty map in order to remove corrupted values from the elevation map. Another useful mechanism is the weighted median filter that enables filling-in of the unseen cells with values interpolated from the neighboring cells of known elevation.

We implemented the CAS filter in our mapping system and tested it sucessfully using the data from the structured light sensor [13]. However, during tests of the mapping system with the URG-04LX scanner on various obstacles the CAS filter failed to remove most of the elevation map artifacts due to mixed measurements. Different spatial characteristics of the mixed range measurements in the ToF-based LMS 200 used in [26], and the phase-shift-based URG scanner are a possible explanation of this behaviour. Because of the range–intensity coupling phenomenon [1] in the phase-shift-based sensor the mixed measurements can appear not only between the two surfaces being observed, but also behind the farther object, or in front of the closer object. This may be a reason for false updates in the certainty map, and henceforth the erratic behaviour of the CAS filter, which unnecessarily deletes the elevation values in some cells of the map on the basis of their low certainty and a lack of spatial continuity in the elevation map and the certainty map.

For that reason the CAS filter algorithm rule for removing the artifacts is not used with the URG-04LX sensor. However, the weighted median filter proposed as the mechanism that fills-in the missing data is still used. The output h_{wm} of the filter is assigned to each cell in the elevation map that is unknown, i.e., has the value of $c^{[i,j]}=0$.

$$h^{[i,j]} = \begin{cases} h_{\text{wm}}^{[i,j]} & \text{if } c^{[i,j]} = 0 \\ h^{[i,j]} & \text{otherwise.} \end{cases}$$

(11)

This mechanism enables to fill-in small portions of the elevation map that are invisible to the sensor due to occlusions.

Because the CAS filter is unable to remove the artifacts due to mixed measurements, the erroneous range data
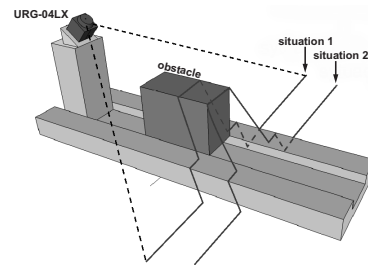

Fig. 11. Typical causes of mixed pixels in terrain profile acquisition.

should be eliminated at the pre-processing stage to avoid erratic behaviour of the map-building procedure. The methods for detection of mixed measurements known from the literature require the intensity information [1], or they are based on accumulation of the range evidence in some form of local environment representation [24]. Unfortunately, the intensity output is not available, and it is not possible to accumulate the range measurements, because the scanner beam sweeps the terrain in front of the robot, and most of the points are measured only once.
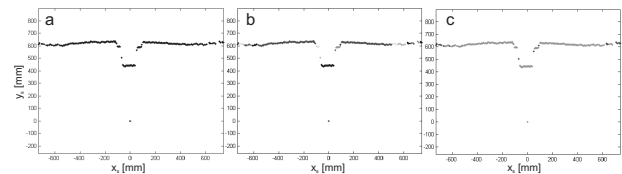

Fig. 12. Removal of mixed measurements by using the clustering approach.

Hence, the spatial and temporal dependencies between the laser scanner measurements in the tilted configuration are exploited to solve the mixed measurements problem. On the basis of our experimental observations it is assumed that typically the mixed measurements arise in two situations (Fig. 11):

1) when a beam hits a very thin object or a sharp edge that is vertical or nearly-parallel to the horizontal direction of the beam,

2) when the laser beam plane aimed downward hits a sharp edge that is roughly perpendicular to the direction of the beams.
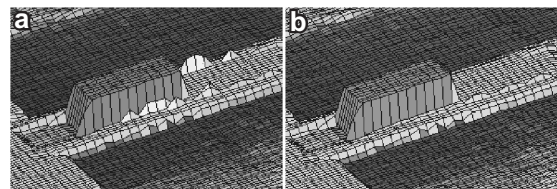

Fig. 13. Example results of the clustering approach to mixed measurements removal.

The first situation results in a single mixed measurement or a small group of points that are spatially isolated. Therefore, such mixed measurements can be removed reliably by clustering the measurements and analyzing discontinuities in the scanned sequence. We use the Range Clustering algorithm proposed in our previous work [23],

which is computationally efficient and based on the underlying physics of the laser range measurements. Figure 12a shows a single scan taken by the tilted URG-04LX scanner (which is located in the origin of the coordinate system). The range measurements belonging to this scan are then clustered, and separated groups are indicated by different shades of gray in Fig. 12b. The same sequence of measurements is shown in Fig. 12c with the small and isolated groups removed (marked in dark gray). Results of using this procedure are shown in Fig. 13, where the artifacts visible in the elevation map (Fig. 13a) on the sides of the box disappear when the mixed measurements are removed from the input data (Fig. 13b).
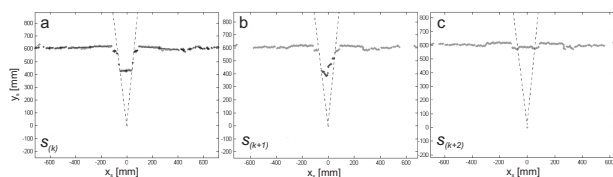

Fig. 14. Removal of mixed measurements by analysing the consecutive scans.

In the second situation described above the group of mixed pixels might be large, and appear as an extension of the actual structures detected by the sensor. To fight out these spurious measurements we check spatial continuity between three neighboring scans: $s_{(k-1)}$, $s_{(k)}$, and $s_{(k+1)}$. At first, we convert the range measurements to the 2D points in the scanner coordinates, and extract groups of co-linear points from the first scan $s_{(k-1)}$, looking for structures that might be edges roughly perpendicular to the scanning direction (Fig. 14a). If such a structure is found, we define an angular sector of measurements that contains this structure. Then, we check the scattering of points along the vertical direction in the second scan $s_{(k)}$ (Fig. 14b) by computing the standard deviation:

$$\sigma^y_{s(k,j)} = \sqrt{\frac{\sum_{i=p_l}^{p_r}(\overline{y}_{s(k,j)} - y^i_{s(k,j)})^2}{p}}, \qquad (12)$$

where $y^i_{s(k,j)}$ is the coordinate of the i-th point in the j-th sector of the k-th scan, $\overline{y}_{s(k,j)}$ is the mean y_s value in the considered angular sector, while p_l and p_r are limits of this sector, and p is the total number of points within these limits. If points in the sector of scan $s_{(k)}$ that was identified as containing an edge have the standard deviation of their y_s values much bigger than the same parameter computed for the scan $s_{(k+1)}$, next in a sequence (Fig. 14c), they are treated as mixed pixels and removed.

This method effectively removes mixed measurements that appear behind obstacles having sharp horizontal edges, which is visible in the example given in Fig. 15. The artifacts caused by a group of mixed measurements (Fig. 15a) are removed without destroying the shape of the mapped object (Fig. 15b).

6. Experimental results

6.1. Controlled environment experiments

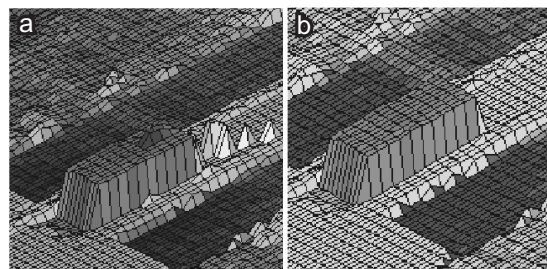Preliminary tests of the mapping system were performed on a simple test bed, constructed in order to make

Fig. 15. Example results of the mixed measurements removal using scan sequence analysis.

these tests independent from the robot pose estimate errors. The test bed consists of a rail with a meter on its side, and a sliding cart (of the same height as the robot) that has the range sensor mounted on it, and can be positioned manually anywhere along the rail. Two versions of the cart were built, one equipped with the complete structured light sensor designed for the Ragno robot (Fig. 16a), and another one with the URG-04LX scanner attached in the same configuration as on the Messor robot (Fig. 16b).
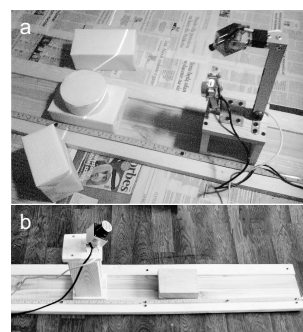

Fig. 16. Simple cart/rail system for tests of the range sensors.

An example of the results obtained with the structured light sensor is shown in Fig. 17. As it can be seen in this figure, the elevation map closely resembles the shape of the boxes used in the experiment (cf. Fig. 16a). Note that the CAS filter has successfully filled-in any missing data preserving the shapes.
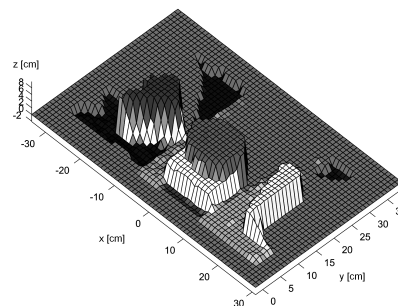

Fig. 17. Elevation map obtained with the structured light sensor.

Similar objects were used to test the mapping software with the Hokuyo URG-04LX (Fig. 18a). As it can be seen in Fig. 18b, the obtained elevation map contains many artifacts caused by mixed measurements. However, if the pre-processing algorithms proposed in Section 5.3

are applied, the shapes of the mapped objects look very much like the boxes and cylinder used in the experiment (Fig. 18c).
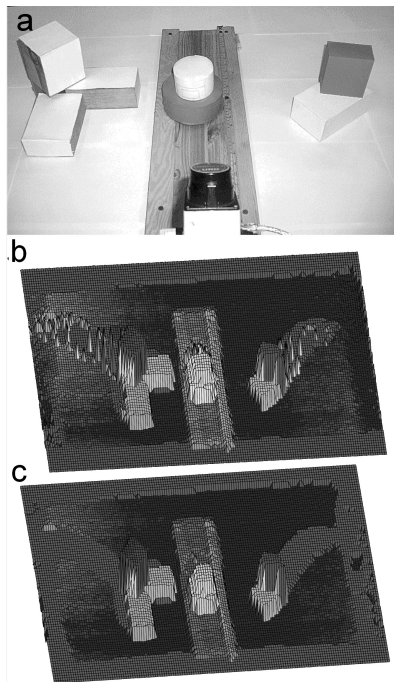

Fig. 18. Elevation maps obtained with the URG-04LX sensor.

In order to compare qualitatively and quantitatively the quality of the elevation maps obtained using the two investigated terrain sensors an experiment in controlled environment was performed. The same scene with some objects of different types was scanned with both sensors moved on the cart/rail system. The measurements were obtained each 10 mm of the rail. The main object in the scene, consisting of two wooden boxes was measured by hand to have the ground truth that can be compared with the maps (Fig. 19).
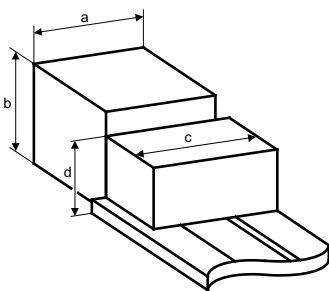

Fig. 19. Boxes measured by the structured light sensor and the URG-04LX sensor.

Figure 20a shows the elevation map obtained using the structured light sensor, while the elevation map of the same scene produced from the laser scanner range data is depicted in Fig. 20b. Comparing the maps qualitatively, one can see that the URG scanner provides much wider field of view, being able to yield range data also describing the smaller objects on the sides of the rail. The field of view of the structured light sensors is narrow, what is a side-effect of the tilted sensor configuration. The spatial resolution

of the structured light measurements depends on the area in which the measured object is located in the perceived image – note that the rail, which appears in the very bottom part of the image, is practically indistinguishable in the elevation map in Fig. 20a, however it is clearly visible in the map obtained from the laser scanner data (Fig. 20b). On the other hand, the surfaces of the boxes in the elevation map produced from the structured light data are smoother. The values in the neighboring cells in the map from the laser scanner data differ much more, what is caused by different measurement errors for surfaces having slightly different brightness.
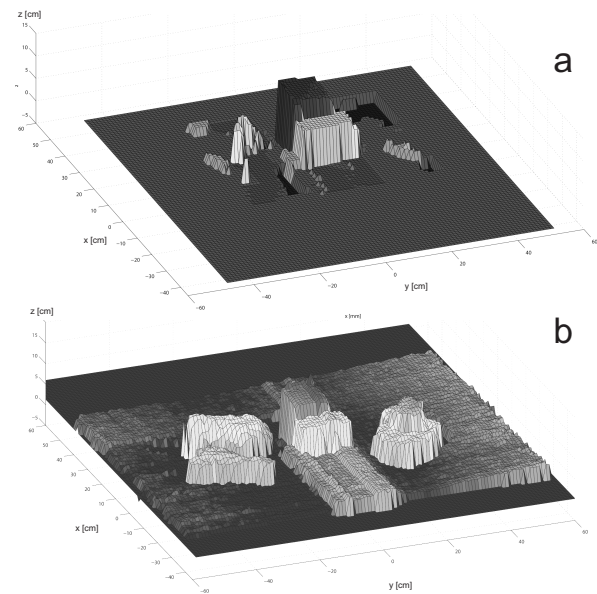

Fig. 20. Comparison of the elevation maps obtained with both sensing modalities.

Quantitative results of the comparison are presented in Tab. 1. The dimensions given in the table are those shown in Fig. 19. The measurements errors are shown as relative values. The elevation map built using the URG-04LX sensor data is more accurate with regard to all, but one measured dimension.

Tab. 1. Comparison of the maps obtained using the structured light system and the URG scanner.

Dim.	Ground truth	Structured light		URG-04LX scanner	
		result	error	result	error
	[mm]	[mm]	[%]	[mm]	[%]
a	103	120	16.5	110	6.8
b	115	126.6	10.0	120.8	5.0
c	154	160	3.9	150	-2.6
d	78	81.3	4.2	91.8	17.7

It was also tested how the sensors behave under different light conditions. All the experiments presented in this article were performed indoors, in the lab, avoiding direct sunlight and light spots from the incandescent bulbs. Under these conditions the structured light system works reliably (Fig. 21a), however if the light is stronger, the laser stripe becomes hardly recognizable in the images (Fig. 21b). This

makes the structured light system unusable outdoors, where any control over the ambient light is not possible. In contrary the URG-04LX scanner shows almost no dependency between the quality of the range measurements and the level of ambient light (Fig. 21c), what is in accordance with the results provided in [8].
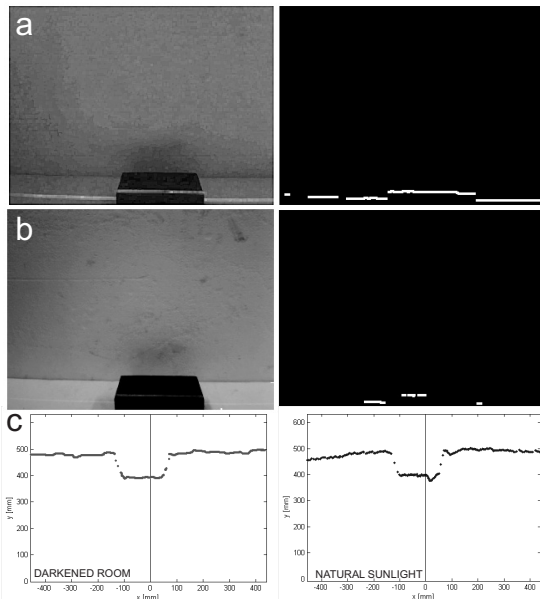

Fig. 21. Comparison of the structured light system performance under different lighting conditions.

6.2. Terrain mapping experiments

The experiments in controlled environment (discussed also in [13] and [15]) ensured us that both the structured light sensor and the laser scanner yield range measurements that are precise enough to be used in mapping applications.
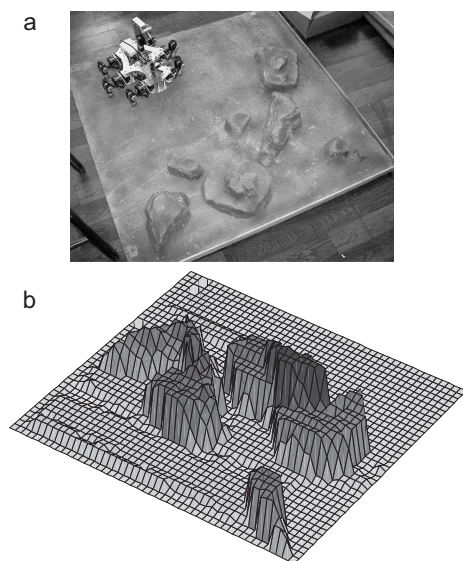

Fig. 22. Uneven terrain experiment and 3D view of the obtained map.

The structured light sensor was used on the small Ragno robot, which does not have an on-board PC, and its autonomy is therefore quite limited. However, the preliminary

terrain mapping experiments with the Ragno robot, performed on a rocky terrain mockup (Fig. 22a) provided evidence that the map updating algorithm works properly on irregular obstacles, and is robust to small errors in the robot localization. Because the robot used only its proprioceptive sensors (accelerometers) for positioning, the covered distance was quite short and limited to the nearly-flat part of the mockup. Nevertheless, the robot has built an elevation map that correctly represents all obstacles in the field of view and is largely free from artifacts (Fig. 22b).
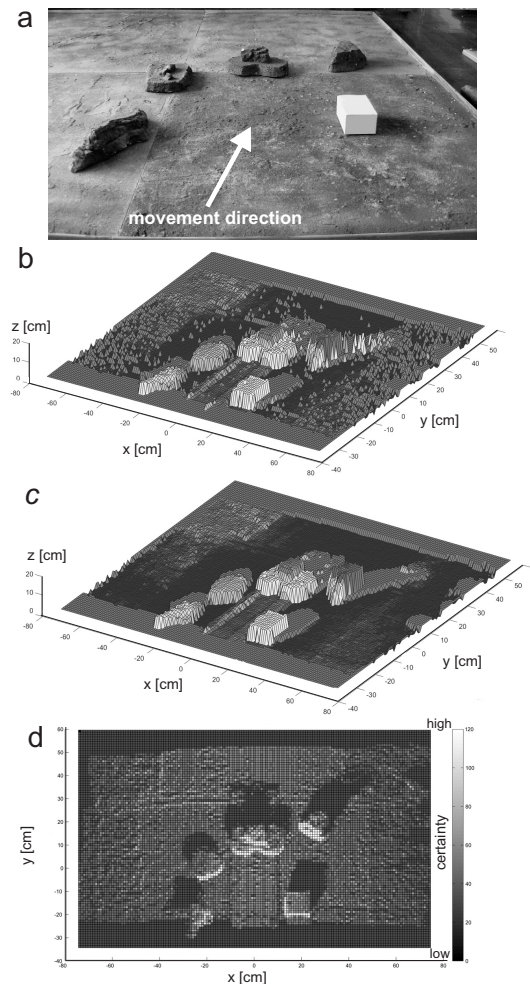

Fig. 23. Elevation and certainty maps obtained on the rocky terrain mockup.

First experiments aimed at testing the Hokuyo URG-04LX on the rocky terrain mockup were performed using the cart/rail setup, in order to separate the adverse effects of robot positioning errors from the errors caused by spurious range measurements (Fig. 23a). Using directly the mapping algorithm from [26] the system built an elevation map that reasonably represents the objects in the scanner's field of view, but contains a number of artifacts (Fig. 23b). These artifacts are mostly caused by mixed measurements behind obstacles and on their sides. There are also many cells that have no valid elevation value set. The elevation map built using our modified method, which relies on range data preprocessing to eliminate spurious measurements and applies the weighted median filter to fill-in the unobserved cells is almost free from artifacts (Fig. 23c). The certainty map (Fig. 23d) contains regions of very low certainty behind

larger obstacles. These areas were never observed by the sensor due to occlusions, and they are too large to be filled-in by the median filter.
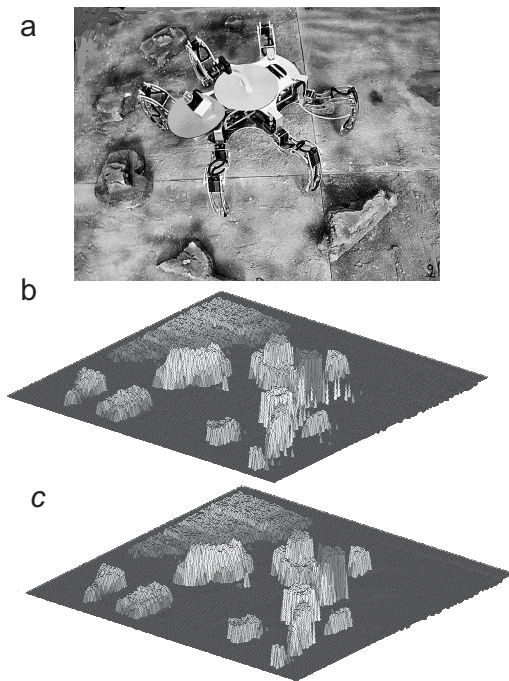

Fig. 24. Messor on a terrain mockup and elevation maps obtained in the experiment.

Also mapping experiments with the Messor robot were performed on the rocky terrain mockup of 2×2 m size. A ceiling-mounted camera was used to obtain an estimate of the horizontal translation and the yaw angle θ_r (robot orientation), while the φ_r (pitch) and ψ_r (roll) angles were provided by the inertial measurement unit of the robot. The colored circles visible on the robot (Fig. 24a) form a landmark used by the vision system. The elevation maps obtained in this experiment acknowledge the results from the cart/rail experiments. The elevation map built with the CAS filter has many peak-like artifacts behind the observed objects (Fig. 24b). These artifacts are not present when the range data pre-processing is applied (Fig. 24c). Although this elevation map correctly represents all encountered obstacles, it is slightly distorted due to the imprecise pose estimates obtained by the robot. Unfortunately, at the moment of preparing this paper there was no precise ground truth available for the rocky terrain mockup. Obtaining such a ground truth requires scanning of the whole mockup with a precisely moved sensor (e.g., mounted on a manipulator), which was not possible so far.

7. Conclusions

This work presents a modified version of the Ye and Borenstein mapping algorithm that contains new artifact removal procedures and is appropriate for a walking robot with a 2D sensor providing sparse range data. Mapping precision of the proposed method is shown in controlled environment experiments with a simple cart/rail test bed, while its potential for real applications is demonstrated with the two walking robots, Ragno and Messor.

Experimental results proved that both 2D range sensors under study are precise enough for terrain mapping, but the reliability and much wider field of view of the laser scanner suggest that the URG-04LX should be the sensor of choice for our Messor robot. On the other hand, the low-cost structured light sensor is a reasonable choice for small educational robots, like the Ragno.

Developing the terrain perception and mapping system with the Hokuyo URG scanner we achieved our main goal: the terrain map is built on-line, on the on-board PC (a low-power Intel Atom machine) of the Messor robot, which is an enabling factor for the autonomy of this robot. The results of using the obtained elevation maps for foothold selection were already shown elsewhere [2].

AUTHORS

Przemysław Łabęcki – Poznań University of Technology, Institute of Control and Information Engineering, ul. Piotrowo 3A, 60-965 Poznań, Poland, e-mail: `pl@cie.put.poznan.pl`

Dawid Rosiński – Poznań University of Technology, Institute of Control and Information Engineering, ul. Piotrowo 3A, 60-965 Poznań, Poland, e-mail: `dawid.rosinski@gmail.com`

Piotr Skrzypczyński* – Poznań University of Technology, Institute of Control and Information Engineering, ul. Piotrowo 3A, 60-965 Poznań, Poland, e-mail: `piotr.skrzypczynski@put.poznan.pl`

* Corrresponding author

References

[1] M. D. Adams, *Sensor modelling, design and data processing for autonomous navigation*. Singapore, World Scientific 1999.

[2] D. Belter, P. Łabęcki, P. Skrzypczyński, Map-based adaptive foothold planning for unstructured terrain walking. *Proc. IEEE Int. Conf. on Robot. and Automat.*, Anchorage, 2010, pp. 5256–5261.

[3] D. Belter, K. Walas, Messor – versatile walking robot for search and rescue missions, *Journal of Automation, Mobile Robotics and Intelligent Systems*, 5(2), 2011, pp. 28–34.

[4] B. Gaßmann, L. Frommberger, R. Dillmann, K. Berns, Real-time 3D map building for local navigation of a walking robot in unstructured terrain, *Proc. IEEE Int. Conf. on Intelligent Robots and Systems*, Las Vegas, 2003, pp. 2185–2190.

[5] B. Gaßmann, J. M. Zöllner, R. Dillmann, Navigation of walking robots: localisation by odometry. *Climbing and Walking Robots VIII*, Berlin, Springer 2005, pp. 953–960.

[6] D. Ilstrup, G. H. Elkaim, Low Cost, low power structured light based obstacle detection, *Proc. IEEE/ION Position, Location and Navigation Symp.*, Monterey, 2008, pp. 771–778.

[7] H. Kawata, A. Ohya, S. Yuta, W. Santosh, T. Mori, Development of ultra-small lightweight optical range sensor system, *Proc. IEEE/RSJ Int. Conf. on Intell.*

Robots and Systems, Edmonton, 2005, pp. 1078–1083.

[8] L. Kneip, F. Tache, G. Caprari, R. Siegwart, Characterization of the compact Hokuyo URG-04LX 2D laser range scanner, *Proc. IEEE Int. Conf. on Robotics and Automation*, Kobe, 2009, pp. 1447–1454.

[9] J. Z. Kolter, Y. Kimz, A. Y. Ng, Stereo vision and terrain modeling for quadruped robots, *Proc. IEEE/RSJ Int. Conf. on Intelligent Robots and Systems*, Kobe, 2009, pp. 1557–1564.

[10] E. Krotkov, R. Hoffman, Terrain mapping for a walking planetary rover. *IEEE Trans. Robot. and Automat.*, 10(6), 1994, pp. 728–739.

[11] V.-G. Loc, S. Roh, I.-M. Koo, D.-T. Tran, H.-M. Kim, H. Moon, H.-R. Choi, Sensing and gait planning of quadruped walking and climbing robot for traversing in complex environment, *Robotics and Autonomous Systems*, 58(5), 2010, pp. 666–675.

[12] P. Łabęcki, A. Kasiński, An active vision system for a walking robot, *Pomiary Automatyka Kontrola*, 55(9), 2009, pp. 731–736 (in Polish).

[13] P. Łabęcki, A. Łopatowski, P. Skrzypczyński, Terrain perception for a walking robot with a low-cost structured light sensor, *Proc. European Conf. on Mobile Robots*, Dubrovnik, 2009, pp. 199–204.

[14] P. Łabęcki, Analysis and optimization of a structured light sensor configuration for terrain map building, *Studies in Automation and Information Technology*, 34, 2009, pp. 37–56 (in Polish).

[15] P. Łabęcki, D. Rosiński, P. Skrzypczyński, Terrain perception and mapping in a walking robot with a compact 2D laser scanner, in: *Emerging Trends in Mobile Robotics* (H. Fujimoto *et al.*, eds.), Singapore, World Scientific 2010, pp. 981–988.

[16] L. Matthies, T. Balch, B. Wilcox, Fast optical hazard detection for planetary rovers using multiple spot laser triangulation, *Proc. IEEE Int. Conf. Robotics and Automation*, 1997, Albuquerque, pp. 859–866.

[17] C. Mertz, J. Kozar, J. Miller, C. Thorpe, Eye-safe laser line striper for outside use, *Proc. IEEE Intell. Vehicle Symp.*, 2002, vol. 2, pp. 507–512.

[18] Y. Okubo, C. Ye, J. Borenstein, Characterization of the Hokuyo URG-04LX laser rangefinder for mobile robot obstacle negotiation. *Unmanned Systems Technology XI*, Proc. SPIE 7332, 2009 (on-line).

[19] C. Plagemann, S. Mischke, S. Prentice, K. Kersting, N. Roy, W. Burgard, Learning predictive terrain models for legged robot locomotion, *Proc. IEEE/RSJ Int. Conf. Intell. Robots and Systems*, Nice, 2008, pp. 3545–3552.

[20] J. Poppinga, A. Birk, K. Pathak, A Characterization of 3D sensors for response robots. *RoboCup 2009: Robot Soccer World Cup XIII* (red. J. Baltes et al.), LNAI Vol. 5949, Berlin, Springer 2010.

[21] A. Roennau, T. Kerscher, M. Ziegenmeyer, J. M. Zöllner, R. Dillmann, Six-legged walking in rough terrain based on foot point planning, in: *Mobile Robotics: Solutions and Challenges* (O. Tosun *et al.*, eds.), Singapore, World Scientific, 2009, pp. 591–598.

[22] A. Schmidt, A. Kasiński, The visual SLAM system for a hexapod robot, in: *Computer Vision and Graphics* (L. Bolc *et al.*, eds.), LNCS Vol. 6375, Berlin, Springer, 2010, pp. 260–267.

[23] P. Skrzypczyński, *Perception uncertainty management in a mobile robot navigation system*, Poznań, Wyd. Politechniki Poznańskiej 2007 (in Polish).

[24] P. Skrzypczyński, On qualitative uncertainty in range measurements from 2D laser scanners, *Journal of Automation, Mobile Robotics and Intelligent Systems*, 2(2), 2008, pp. 35–42.

[25] K. Walas, D. Belter, A. Kasiński, Control and environment sensing system for a six-legged robot, *Journal of Automation, Mobile Robot. & Intell. Syst.*, 2(3), 2008, pp. 26–31.

[26] C. Ye, J. Borenstein, A novel filter for terrain mapping with laser rangefinders. *IEEE Trans. Robot. and Automat.*, 20(5), 2004, pp. 913–921.